3α clustering in excited states of ^{16}C

T. Baba, Y. Chiba, and M. Kimura
Department of Physics, Hokkaido University, 060-0810 Sapporo, Japan
(Received 2 October 2014; revised manuscript received 4 November 2014; published 29 December 2014)

The α-cluster states of ^{16}C are investigated by using antisymmetrized molecular dynamics. It is shown that two different types of α-cluster states exist: triangular and linear-chain states. The former has an approximate isosceles triangular configuration of α particles surrounded by four valence neutrons occupying the sd shell, while the latter has the linearly aligned α particles with $(sd)^2(pf)^2$ neutrons. It is found that the structure of the linear-chain state is qualitatively understood in terms of the $3/2^-_\pi$ and $1/2^-_\sigma$ molecular orbits as predicted by molecular-orbital model, but there exists a non-negligible $^{10}\mathrm{Be}+\alpha+2n$ correlation. The bandhead energies of the triangular and linear-chain rotational bands are 8.0 and 15.5 MeV, and the latter is close to the ^{4}He $+^{12}$Be and ^{6}He $+^{10}$Be threshold energies. It is also shown that the linear-chain state becomes the yrast state at $J^\pi = 10^+$ with $E_x = 27.8$ MeV owing to its very large moment of inertia comparable with hyperdeformation.

DOI: 10.1103/PhysRevC.90.064319 PACS number(s): 27.20.+n, 23.20.−g, 21.10.Re

I. INTRODUCTION

The excited states of atomic nuclei, especially those of light nuclei, show strong α clustering, and many different types of α-cluster structure appear as the excitation energy increases [1–5]. In particular, the linear-chain configuration of three α particles (three linearly aligned α particles) suggested by Morinaga [6] has long been an important and interesting subject because of its exotic structure and large deformation, equivalent to hyperdeformation. The Hoyle state (0^+_2 state of ^{12}C) was the first candidate of the linear chain, but later it turned out that it does not have the linear-chain configuration but consists of loosely coupled 3α particles with dilute gaslike nature [7–10]. In turn, the instability of the linear-chain configuration against the bending motion (deviation from linear alignment) was pointed out and the bent-armed configuration was predicted by the antisymmetrized molecular dynamics (AMD) [11] and Fermionic molecular dynamics (FMD) calculations [12].

The interest in the linear-chain state is reinforced by the unstable nuclear physics, because the addition of the valence neutrons will increase the stability of α-cluster structure by their gluelike role. For example, 2α-cluster structures of Be isotopes are assisted by valence neutrons that are well described in terms of the molecular orbits [13–18]. Naturally, we expect that the linear-chain configurations of 3α clusters can be stabilized by the assistance of valence neutrons in neutron-rich C isotopes. Indeed, there are a number of studies to theoretically predict and experimentally search for the linear-chain states in neutron-rich carbon isotopes [19–27]. Among C isotopes, ^{16}C is a very interesting and important nucleus as the most promising candidate of the stable linear-chain state, because its stability against the bending motion was pointed out by molecular-orbital model calculation [19]. Assuming a 3α cluster core and $3/2^-_\pi$, $1/2^-_\pi$, and $1/2^-_\sigma$ molecular orbits of valence neutrons, it was shown that the linear-chain configuration with valence neutrons occupying $(3/2^-_\pi)^2(1/2^-_\sigma)^2$ molecular orbits is stable. Therefore, it is very important and interesting to investigate the linear-chain state in ^{16}C without an *a priori* assumption on the cluster core and valence neutron orbits. Furthermore, in addition to the linear-chain configuration, triangular configurations of 3α particles are also suggested in the neighboring nuclei such as ^{13}C and ^{14}C [26–29]. Therefore, it is also interesting to search for an analogous state in ^{16}C.

For this purpose, we discuss 3α cluster states in ^{16}C based on AMD, which has been successfully applied to the studies of the clustering in unstable nuclei [17,18,30–32]. Our aim in the present study is twofold. The first is to search for and show the linear chain and other cluster states in ^{16}C without an *a priori* assumption on the structure and to test the stability against the bending motion. We show that two different types of the 3α cluster states exist, triangular and linear-chain configurations. It is also shown that the valence neutron orbits are qualitatively understood in terms of the molecular orbits, and the linear-chain configuration is stable with the help of those valence neutrons. The second aim is to provide a quantitative and reliable prediction of their properties for the experimental survey. We predict the bandhead states of the triangular and linear-chain bands at 8.0 and 15.5 MeV, and the $J^\pi = 10^+$ state of the linear-chain configuration becomes the yrast state at $J^\pi = 10^+$ with $E_x = 27.8$ MeV owing to its very large moment of inertia comparable with hyperdeformation.

II. THEORETICAL FRAMEWORK

A. Variational calculation and generator coordinate method

The microscopic A-body Hamiltonian used in this study is written as

$$\hat{H} = \sum_{i=1}^{A} \hat{t}(i) + \sum_{i<j}^{A} \hat{v}_n(ij) + \sum_{i<j}^{Z} \hat{v}_C(ij) - \hat{t}_{\mathrm{c.m.}}, \qquad (1)$$

where the Gogny D1S interaction [33] is used as an effective nucleon-nucleon interaction $\hat{v}_n$ and the Coulomb interaction $\hat{v}_C$ is approximated by a sum of seven Gaussians. The center-of-mass (c.m.) kinetic energy $\hat{t}_{\mathrm{c.m.}}$ is exactly removed.

The intrinsic wave function Φ_{int} of the system is represented by a Slater determinant of single-particle wave packets, and we employ the parity-projected wave function Φ^π as the

variational wave function,

$$\Phi^{\pi} = \frac{1+\pi\hat{P}_x}{2}\Phi_{\rm int}, \quad \Phi_{\rm int} = \mathcal{A}\{\varphi_1,\varphi_2,\ldots,\varphi_A\}, \tag{2}$$

where φ_i is the single-particle wave packet which is a direct product of the deformed Gaussian spatial [34], spin (χ_i), and isospin (ξ_i) parts,

$$\varphi_i(\mathbf{r}) = \exp\left\{-\sum_{\sigma=x,y,z}\nu_\sigma\left(r_\sigma - \frac{Z_{i\sigma}}{\sqrt{\nu_\sigma}}\right)^2\right\}\chi_i\xi_i,$$
$$\chi_i = a_i\chi_\uparrow + b_i\chi_\downarrow, \quad \xi_i = \text{proton or neutron}. \tag{3}$$

In this study, we focus on the positive-parity states of ^{16}C. The parameters $\boldsymbol{Z}_i$, a_i, b_i, and ν_σ are optimized by the variational calculation explained below. To investigate 3α cluster states, we first perform the variational calculation with the constraint on the quadrupole deformation parameter β. In this calculation, we do not impose a constraint on the parameter γ, and hence, thus-obtained wave functions have γ values that give the largest binding energies for given values of β. As shown in the next section, we have obtained the linear-chain configuration located at $(\beta,\gamma) = (1.10,0)$ as well as the triangular configuration. We performed another variational calculation to test its stability against bending motion (deviation from the linear alignment of 3α clusters). Namely, starting from the above mentioned linear-chain configuration, we gradually increased the parameter γ keeping $\beta = 1.10$ by applying the constraints on β and γ simultaneously. This calculation generates the energy curve of the linear-chain configuration as function of γ.

After the variational calculation, the eigenstate of the total angular momentum J is projected out from the wave functions Φ_i^+ obtained by variational calculations,

$$\Phi^{J+}_{MKi} = \frac{2J+1}{8\pi^2}\int d\Omega D^{J*}_{MK}(\Omega)\hat{R}(\Omega)\Phi_i^+. \tag{4}$$

Here, $D^J_{MK}(\Omega)$ is the Wigner D function and $\hat{R}(\Omega)$ is the rotation operator. The integrals over three Euler angles Ω are evaluated numerically. Then, we perform generator coordinate method (GCM) by employing the quadrupole deformation parameter β as the generator coordinate. The wave functions Φ^{J+}_{MKi} are superposed,

$$\Psi^{J+}_{M\alpha} = \sum_{Ki} g^J_{Ki\alpha}\Phi^{J+}_{MKi}, \tag{5}$$

where the coefficients $g^J_{Ki\alpha}$ and eigenenergies E^{J+}_α are obtained by solving the Hill-Wheeler equation [35],

$$\sum_{i'K'} H^{J+}_{KiK'i'}g^J_{K'i'\alpha} = E^{J+}_\alpha\sum_{i'K'}N^{J+}_{KiK'i'}g^J_{K'i'\alpha}, \tag{6}$$
$$H^{J+}_{KiK'i'} = \left\langle\Phi^{J+}_{MKi}\middle|\hat{H}\middle|\Phi^{J+}_{MK'i'}\right\rangle, \tag{7}$$
$$N^{J+}_{KiK'i'} = \left\langle\Phi^{J+}_{MKi}\middle|\Phi^{J+}_{MK'i'}\right\rangle. \tag{8}$$

The wave functions $\Psi^{J+}_{M\alpha}$ that describe the ground and excited states of ^{16}C are called GCM wave function in the following.

B. Single-particle orbits

To investigate the motion of the valence neutrons around the core nucleus, we calculate the neutron single-particle orbits of the intrinsic wave function. We first transform the single-particle wave packet φ_i of each optimized intrinsic wave function $\Phi_{\rm int}$ to the orthonormalized basis,

$$\widetilde{\varphi}_\alpha = \frac{1}{\sqrt{\lambda_\alpha}}\sum_{i=1}^{A}c_{i\alpha}\varphi_i. \tag{9}$$

Here, λ_α and $c_{i\alpha}$ are the eigenvalues and eigenvectors of the overlap matrix $B_{ij} = \langle\varphi_i|\varphi_j\rangle$. Using this basis, the Hartree-Fock single-particle Hamiltonian is derived,

$$h_{\alpha\beta} = \langle\widetilde{\varphi}_\alpha|\hat{t}|\widetilde{\varphi}_b\rangle + \sum_{\gamma=1}^{A}\langle\widetilde{\varphi}_\alpha\widetilde{\varphi}_\gamma|\hat{v}_n + \hat{v}_C|\widetilde{\varphi}_\beta\widetilde{\varphi}_\gamma - \widetilde{\varphi}_\gamma\widetilde{\varphi}_\beta\rangle,$$
$$+\frac{1}{2}\sum_{\gamma,\delta=1}^{A}\langle\widetilde{\varphi}_\gamma\widetilde{\varphi}_\delta|\widetilde{\varphi}^*_\alpha\widetilde{\varphi}_\beta\frac{\delta\hat{v}_n}{\delta\rho}|\widetilde{\varphi}_\gamma\widetilde{\varphi}_\delta - \widetilde{\varphi}_\delta\widetilde{\varphi}_\gamma\rangle. \tag{10}$$

The eigenvalues ϵ_s and eigenvectors $f_{\alpha s}$ of $h_{\alpha\beta}$ give the single-particle energies and the single-particle orbits, $\widetilde{\phi}_s = \sum_{\alpha=1}^{A}f_{\alpha s}\widetilde{\varphi}_\alpha$. To discuss the properties of the single-particle levels, we also calculate the amount of the positive-parity component,

$$p^+ = |\langle\widetilde{\phi}_s|\frac{1+P_x}{2}|\widetilde{\phi}_s\rangle|^2, \tag{11}$$

and angular momenta in the intrinsic frame,

$$j(j+1) = \langle\widetilde{\phi}_s|\hat{j}^2|\widetilde{\phi}_s\rangle, \quad |j_z| = \sqrt{\langle\widetilde{\phi}_s|\hat{j}_z^2|\widetilde{\phi}_s\rangle}, \tag{12}$$
$$l(l+1) = \langle\widetilde{\phi}_s|\hat{l}^2|\widetilde{\phi}_s\rangle, \quad |l_z| = \sqrt{\langle\widetilde{\phi}_s|\hat{l}_z^2|\widetilde{\phi}_s\rangle}. \tag{13}$$

III. RESULTS AND DISCUSSIONS

A. 3α clustering and valence neutron configurations on the energy curve

Figure 1 shows the energy curves as functions of quadrupole deformation parameter β for $J^\pi = 0^+$ states obtained by the variational calculation with the constraint on the parameter β. The filled symbols show the energy minimum for given values of β, and on this energy curve, three different structures appear, which are shown by circles, triangles, and boxes. These structures are also obtained as the local energy minima above the lowest energy states and are shown by open symbols. It is also noted that there are other local energy minima with different structures above the energy curve. They do not have cluster structure and are not shown in Fig. 1, but are included as the basis wave function of the GCM calculation. We first discuss three different structures with and without clustering that appear on the energy curve by referring their density distributions (Fig. 2) and the properties of valence neutron orbits (Table I). The lowest energy configuration shown by circles is prolately deformed and has the minimum at $E = -110.4$ MeV and $(\beta,\gamma) = (0.44,0)$. As seen in its proton and valence neutron density distribution [Figs. 2(a) and 2(b)], it has no pronounced clustering, and four valence neutrons

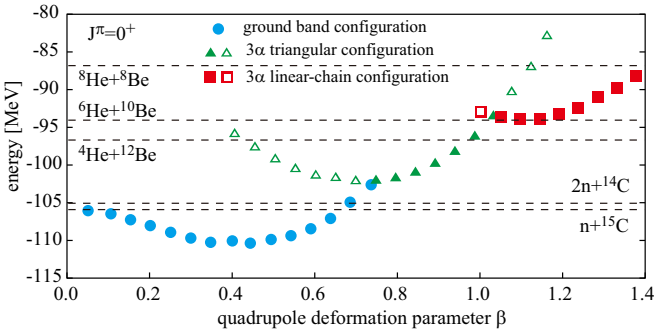

FIG. 1. (Color online) The energy curve of the $J^\pi = 0^+$ states as functions of quadrupole deformation parameter β obtained by the angular momentum projection. Filled symbols show the energy minimum states for given values of β, while open symbols show local energy minima. There appear three different structures shown by circles, triangles, and boxes (see text). Dashed lines show the thresholds energies for $1n$, $2n$, and cluster decays.

have an approximate $(0p_{1/2})^2(0d_{5/2})^2$ configuration that is also confirmed from the properties of neutron single-particle orbits listed in Table I, entries (a) and (b). Namely the first two valence neutrons occupy the orbit (a) with negative parity, $j \simeq 1/2$ and $l \simeq 1$, and the last two neutrons occupy the orbit (b) with positive parity, $j \simeq 5/2$ and $l \simeq 2$. The deviation from the spherical $p_{1/2}$ and $d_{5/2}$ orbits owes to prolate deformation of this state. Different from the AMD results by Kanada-En'yo [36] in which the different proton and neutron deformation of ^{16}C was discussed (i.e., the proton is oblately deformed, while the neutron is prolately deformed), the present result shows that the both proton and neutron are prolately deformed in the ground state. This difference may be attributed to the difference of the effective interaction used in this study and Ref. [36]. It is known that the deformation of the ^{16}C strongly depends on the effective interaction. For example, the Skyrme Hartree-Fock + BCS calculation with SGII interaction [37] reports the almost degenerated prolate and oblate minima, while the relativistic mean-field + BCS calculation using the parameter set of PC-F1 [38] reports the triaxial deformation.

TABLE I. The properties of valence neutron orbits shown in Fig. 2. Each column shows the single-particle energy ε in MeV, the amount of the positive-parity component p^+, and the angular momenta [see Eqs. (11)–(13)].

Orbit	ε	p^+	j	$\lvert j_z\rvert$	l	$\lvert l_z\rvert$
(a)	−8.24	0.00	0.75	0.51	1.05	0.97
(b)	−5.23	0.99	2.21	0.51	1.80	0.38
(c)	−5.74	0.99	2.31	1.96	1.93	1.63
(d)	−3.29	0.98	2.33	1.88	2.07	1.83
(e)	−5.32	0.13	2.09	1.49	1.72	0.99
(f)	−4.18	0.03	2.89	0.53	2.72	0.18

As deformation increases, another valence neutron configuration appears and it induces 3α clustering. A triaxially deformed 3α cluster configuration shown by triangles appears around $\beta = 0.7$ and has the local energy minimum at $E = -102.2$ MeV and $(\beta, \gamma) = (0.70, 41)$. At the energy minimum, this configuration has 3α cluster core of an approximate

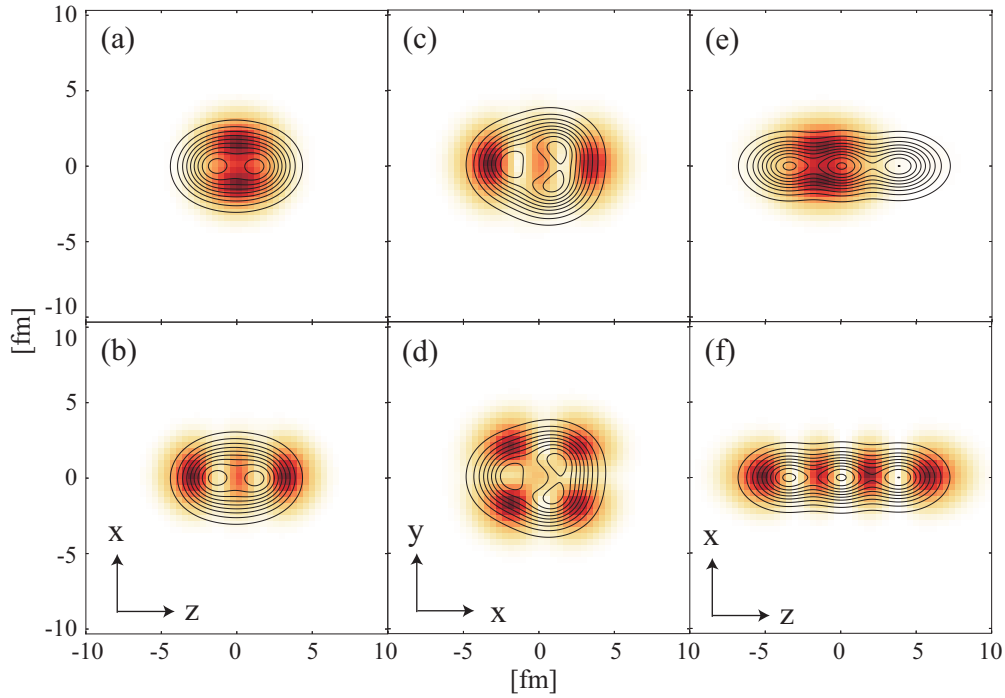

FIG. 2. (Color online) The density distribution of the ground (a,b), triangular (c,d), and linear-chain (e,f) configurations at their energy minima. The contour lines show the proton density distributions and are common to the upper and lower panels. The color plots show the single-particle orbits occupied by four valence neutrons. The lower panels show the most weakly bound two neutrons, while the upper panel show the other two valence neutrons.

isosceles triangular configuration with 3.2-fm long sides and 2.3-fm short side [Figs. 2(c) and 2(d)], which is the origin of the triaxial deformation, and an approximate $(0d_{5/2})^4$ configuration ($2\hbar\omega$ excitation) of valence neutrons is confirmed from Table I. It is also notable that $|j_z|$ of valence neutron orbits deviate from half-integer value because of axial symmetry breaking caused by the triangular configuration. Thus, by increasing the nuclear deformation, the valence neutron configuration changes and it triggers the clustering of the core nucleus. This feature is common to the well-known 2α clustering of Be isotopes and theoretically predicted clustering in O, F, and Ne [30–32] isotopes.

Further increase of nuclear deformation realizes the exotic cluster configuration with the linear alignment of 3α particles, which is denoted by boxes. This configuration has a local minimum at $E = -93.9$ MeV and $(\beta,\gamma) = (1.10,0)$, whose energy is very close to the ^{4}He $+^{12}$Be and ^{6}He $+^{10}$Be cluster thresholds, and the ratio of deformation axis is approximately equal to 3:1. As clearly seen in Figs. 2(e) and 2(f), a linearly aligned 3α cluster core is accompanied by four valence neutrons whose configuration may be roughly understood as $(1p)^2(0f)^2$, although the deviation from ordinary spherical shell is fairly large due to very strong deformation. An alternative and more appropriate interpretation of the valence neutron configuration is given by the molecular orbits. Namely, the valence neutron orbits are in good accordance with the $3/2^-_\pi$ and $1/2^-_\sigma$ orbits [19] that are the linear combinations of the p orbits around α clusters as illustrated in Fig. 3. Indeed, the density distribution and properties of these orbits shown in Fig. 2 are in very good agreement with those of the molecular-orbital model. It is also noted that the $(3/2^-_\pi)^2(1/2^-_\pi)^2$ configuration was not obtained in this study, and hence the present results support the instability of $(3/2^-_\pi)^2(1/2^-_\pi)^2$ configuration and stability of $(3/2^-_\pi)^2(1/2^-_\sigma)^2$ configuration.

Thus, concerning the linear-chain configuration of ^{16}C, the present calculation yielded qualitatively the same conclusion with the molecular-orbital model. However, it is worthwhile to focus on the quantitative differences. The linear-chain configuration obtained in this study has parity asymmetric structure and shows a $^{10}\mathrm{Be}+\alpha+2n$ like correlation, which is analogous to $^{10}\mathrm{Be}+\alpha$ correlation in ^{14}C reported by Suhara *et al.* [39]. Namely, the $3/2^-_\pi$ orbit has non-negligible parity mixing ($p^+ = 0.13$) and is localized between the left and center α clusters showing similar structure to ^{10}Be. Indeed, owing to the gluelike role of the $3/2^-_\pi$ orbit, the distance between the left and center α clusters (3.5 fm) is shorter than that between the right and center (3.8 fm). On the other hand, the $1/2^-_\sigma$ orbit has almost no parity mixing ($p^+ = 0.03$) and distributes around the entire system to bond ^{10}Be and α clusters. Therefore, this state can be alternatively interpreted as $^{10}\mathrm{Be}+\alpha$ clusters accompanied by two covalent neutrons in $1/2^-_\sigma$ orbit. This interpretation may explain why the excitation energy of the linear-chain configuration is much lower than that predicted by the molecular-orbital model and located in the vicinity of the ^{6}He $+^{10}$Be and ^{4}He $+^{12}$Be thresholds. It is evident that the parity projection plays a crucial role to yield this asymmetric internal structure, because we only obtain parity-symmetric intrinsic wave functions if we do not perform parity projection.

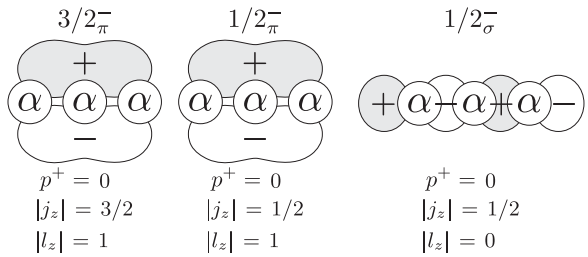

FIG. 3. The schematic figure showing the $3/2^-_\pi$, $1/2^-_\pi$, and $1/2^-_\sigma$ molecular orbits introduced in Ref. [19]. If the system has axial symmetry and the effect of the spin-orbit interaction is negligible, these orbits are the eigenstates of $\hat{j}_z$ and $\hat{l}_z$.

B. Stability of the linear-chain state

One of the main concerns about the linear-chain configuration is its stability against the bending motion, and we confirm it by investigating its response to γ deformation.

Starting from the linear-chain configuration shown in Figs. 2(e) and 2(f), we gradually increased γ but kept β constant by using the constraint on β and γ. Thus the obtained energy curve of the linear-chain configuration with $J^\pi = 0^+$ as function of γ is shown in Fig. 4. It is almost constant for small value of γ and has the minimum at $\gamma = 3.1$ deg but rapidly increases for larger values of γ. Then, including all the basis wave functions, we performed a GCM calculation to obtain the excitation spectrum and band structure, which are discussed in the next subsection. Here, we focus on the bandhead state of the linear-chain band (0^+_5 state) to see the stability against γ deformation. For this purpose, we calculated the overlap between the 0^+_5 state and the basis wave function with γ deformed linear-chain configuration defined as

$$O(\gamma) = |\langle\Psi(0^+_5)|\Phi^{0^+}(\gamma)\rangle|^2. \tag{14}$$

Here, $\Psi(0^+_5)$ and $\Phi^{0^+}(\gamma)$ denote the GCM wave function of the 0^+_5 state and the basis wave function with γ deformed linear-chain configuration shown in Fig. 4. The calculated overlap shown by the solid line in Fig. 4 has its maximum value 0.92 at $\gamma = 3.1$ deg and falls off very quickly as γ

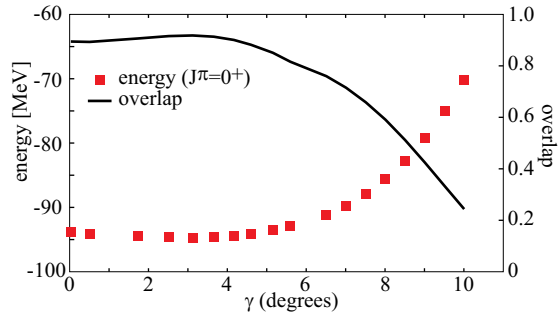

FIG. 4. (Color online) The boxes show the energy of the linear-chain configuration with $J^\pi = 0^+$ as function of quadrupole deformation parameter γ. The solid line shows the overlap between the linear-chain state (0^+_5 state) and the basis wave functions.

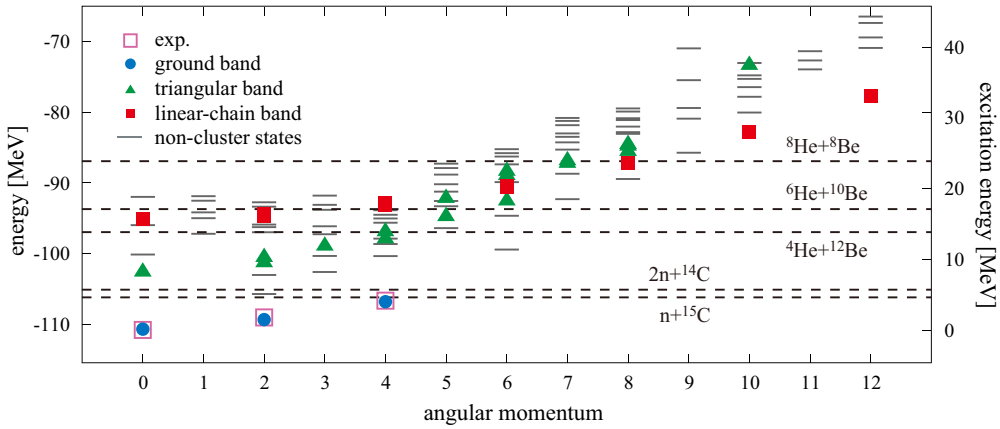

FIG. 5. (Color online) The calculated and observed positive-parity energy levels of ^{16}C up to $J^\pi = 12^+$ states. Open boxes show the observed states with the definite spin-parity assignments, and other symbols show the calculated result. The filled circles, triangles, and lines show the ground, triangular, and linear-chain bands, while lines show the states without cluster structure.

increases. Therefore the wave function of the linear-chain state is well confined within a region of small γ and hence stable against the bending motion. Further extensive investigation of the stability of the linear-chain state including other carbon isotopes will be discussed in our forthcoming paper.

C. Excitation spectrum

Figure 5 shows the spectrum up to $J^\pi = 12^+$ state obtained by the GCM calculation including whole-basis wave functions. We classified the obtained states as the "ground band," "triangular band," "linear-chain band," and other noncluster states based on their $B(E2)$ strengths and the overlap with the basis wave functions. Table II shows the member states of these bands with small angular momenta.

TABLE II. Excitation energies (MeV) and proton and neutron root-mean-square radii (fm) of several member states of the ground band, triangular band, and linear-chain band. Numbers in the parentheses are the observed data.

Band	J^π	E_x	r_p	r_n
Ground	0^+_1	0.0	2.61	2.84
	2^+_1	1.3 (1.77)	2.60	2.83
	4^+_1	3.9 (4.14)	2.56	2.77
Triangular	0^+_2	8.0	2.75	3.09
$K^\pi = 0^+$	2^+_4	9.4	2.74	3.08
	4^+_4	12.7	2.76	3.06
Triangular	2^+_5	10.1	2.74	3.08
$K^\pi = 2^+$	3^+_3	11.7	2.74	3.07
	4^+_6	13.7	2.74	3.08
Linear chain	0^+_5	15.5	3.54	3.71
	2^+_9	15.9	3.14	3.27
	2^+_{10}	16.3	3.38	3.54
	4^+_{11}	17.6	3.22	3.38
	4^+_{12}	17.8	3.21	3.39

The member states of the ground band shown by circles in Fig. 5 are dominantly composed of the basis wave functions with $(sd)^2$ configuration on the energy curve. The ground state has the largest overlap with the basis wave function shown in Figs. 2(a) and 2(b) that amounts to 0.95, and the calculated binding energy is -110.6 MeV, which nicely agrees with the observed value (-110.8 MeV). The excitation energies of the 2^+_1 and 4^+_1 states are also reasonably described. However, our result considerably overestimates the observed $B(E2; 2^+_1 \to 0^+_1)$ strength reported by experiments [40–44] that ranges from 0.92 to 4.2 e^2 fm^4. There have been many discussions about the possible hindrance [36,37,44] of $B(E2)$, and in the case of the AMD study [36], the origin of the hindrance was attributed to the different proton and neutron deformation. On the other hand, the present results does not describe it as mentioned before, and it leads to the overestimation of $B(E2)$ (Table III).

Owing to its triaxial deformed shape, the triangular configuration generates two rotational bands built on the 0^+_2 and 2^+_5 states. We call them $K^\pi = 0^+$ and 2^+ bands in the following, although the mixing of the K quantum number in their GCM wave functions [Eq. (5)] is not negligible. Compared to the linear-chain state, these bands have less pronounced clustering and α clusters are considerably distorted; therefore the bandhead energies are well below the cluster thresholds. The member states have large overlap with the basis wave function shown in Figs. 2(c) and 2(d), which amount to, for example, 0.93 in the case of the 0^+_2 state. However, the member states with larger angular momentum with $J^\pi \geqslant 5^+$ are fragmented into several states due to the coupling with other noncluster configurations. The fragmentation gets stronger as the angular momentum increases, and hence the member states with $J^\pi \geqslant 9$ and band terminal are unclear. Due to larger deformation of the triangular states, the inter- and intraband $B(E2)$ strengths between the $K^\pi = 0^+$ and $K^\pi = 2^+$ bands are enhanced compared to the ground band.

The linear-chain configuration generates a rotational band built on the 0^+_5 state at 15.5 MeV that is close to the ^{4}He + ^{12}Be and ^{6}He + ^{10}Be threshold energies. The bandhead state 0^+_5 has the largest overlap with the basis wave function shown in

TABLE III. The calculated intra- and interband $B(E2; J_i \to J_f)$ (e^2 fm^4) strengths for low-spin member states of the ground, triangular, and linear-chain bands. Transitions less than 5 e^2 fm^4 are not shown.

	$J_i \to J_f$	$B(E2; J_i \to J_f)$
Ground → ground	$2^+_1 \to 0^+_1$	6.0
	$4^+_1 \to 2^+_1$	5.1
Triangular	$2^+_4 \to 0^+_2$	10.9
$K^\pi = 0^+ \to K^\pi = 0^+$	$4^+_4 \to 2^+_4$	15.7
Triangular	$3^+_3 \to 2^+_5$	17.9
$K^\pi = 2^+ \to K^\pi = 2^+$	$4^+_6 \to 3^+_3$	9.5
	$4^+_6 \to 2^+_5$	6.2
Triangular	$2^+_5 \to 0^+_2$	6.9
$K^\pi = 2^+ \to K^\pi = 0^+$	$3^+_3 \to 2^+_4$	10.4
	$3^+_3 \to 4^+_4$	8.3
Linear chain → linear chain	$2^+_9 \to 0^+_5$	58.9
	$2^+_{10} \to 0^+_5$	182.4
	$4^+_{11} \to 2^+_9$	114.3
	$4^+_{11} \to 2^+_{10}$	70.8
	$4^+_{12} \to 2^+_9$	29.5
	$4^+_{12} \to 2^+_{10}$	158.0

Figs. 2(e) and 2(f), which amounts to 0.92, but the member states with $J^\pi = 2^+$, 4^+, and 6^+ are fragmented into two states due to the coupling with other noncluster basis wave functions. For example, the 2^+_9 and 2^+_{10} states respectively have 0.30 and 0.65 overlaps with the basis wave function of Figs. 2(e) and 2(f). By averaging the excitation energies of the fragmented member states, the moment of inertia is estimated as $\hbar/2\Im = 112$ keV. Because of this strong deformation comparable with hyperdeformation, the member states have huge intraband $B(E2)$ values that are larger, in order of magnitude, than those in other bands. Naturally, as the angular momentum increases, the excitation energy of the linear-chain state is lowered relative to other structures, and the $J^\pi = 10^+$ member state at $E_x = 27.8$ MeV becomes the yrast state. Unlike the triangular band, the high-spin member states with $J^\pi \geqslant 8^+$ are not fragmented and the band structure looks rather clear. Since the excitation energy of the high-spin state with linear-chain configuration is relatively lower than others, the coupling with the noncluster states and hence the fragmentation of the states may be hindered. Thus, we predict the stable linear-chain configuration with molecular orbits whose bandhead energy is around ^{4}He $+^{12}$Be and ^{6}He $+^{10}$Be thresholds. Owing to its large moment of inertia, the $J^\pi = 10^+$ member state becomes an yrast state. Those suggest that the linear-chain band might be populated in the ^{4}He $+^{12}$Be and ^{6}He $+^{10}$Be reaction channels.

IV. SUMMARY

We have studied 3α cluster states of ^{16}C based on the AMD calculations. By the variational calculation with the constraint on the quadrupole deformation parameter β, it was found that two different 3α cluster states appear, depending on the magnitude of the deformation and the valence neutron configurations. The triangular configuration of 3α clusters is accompanied by the valance neutrons in a $(sd)^4$ configuration, while the linear-chain configuration has the valence neutrons with a $(sd)^2(pf)^2$ configuration. From the analysis of the neutron single-particle orbits, it is shown that the valence neutron orbits of the linear-chain configuration is understood well in terms of molecular orbits and it is qualitatively in good accordance with the $(3/2^-_\pi)^2(1/2^-_\sigma)^2$ configuration suggested by molecular-orbital model. We also pointed out parity asymmetry of the linear-chain configuration that originates in $^{10}\text{Be} + \alpha + 2n$ cluster nature. The GCM calculation demonstrated that the wave function of the linear-chain state is well confined within a region of small γ, and hence, it is stable against bending motion. We predict the presence of rotational bands associated with 3α cluster states. In particular, the linear-chain band is built in the vicinity of the ^{4}He $+^{12}$Be and ^{6}He$+^{10}$Be thresholds energies, and the $J^\pi = 10^+$ state becomes a yrast state.

ACKNOWLEDGMENTS

Part of the numerical calculations were performed on the HITACHI SR16000 at KEK. One of the authors (M.K.) acknowledges the support by the Grants-in-Aid for Scientific Research on Innovative Areas from MEXT (Grant No. 2404:24105008) and JSPS KAKENHI Grant 563 No. 25400240.

[1] K. Wildermuth and T. Kanellopoulos, Nucl. Phys. **7**, 150 (1958); **9**, 449 (1958/59).
[2] R. K. Sheline and K. Wildermuth, Nucl. Phys **21**, 196 (1960).
[3] Y. Abe *et al.*, Prog. Theor. Phys. Suppl. **68**, 303 (1980).
[4] W. von Oertzen, M. Freer, and Y. Kanada-En'yo, Phys. Rep. **432**, 43 (2006).
[5] H. Horiuchi, K. Ikeda, and K. Kato, Prog. Theor. Phys. Suppl. **192**, 1 (2012).
[6] H. Morinaga, Phys. Rev. **101**, 254 (1956).
[7] E. Uegaki, S. Okabe, Y. Abe, and H. Tanaka, Progr. Theor. Phys. **57**, 1262 (1977); **62**, 1621 (1979).
[8] M. Kamimura, Nucl. Phys. A **351**, 456 (1981).
[9] A. Tohsaki, H. Horiuchi, P. Schuck, and G. Röpke, Phys. Rev. Lett. **87**, 192501 (2001).
[10] Y. Funaki, A. Tohsaki, H. Horiuchi, P. Schuck, and G. Röpke, Phys. Rev. C **67**, 051306 (2003).
[11] Y. Kanada-En'yo, Phys. Rev. Lett. **81**, 5291 (1998).
[12] M. Chernykh, H. Feldmeier, T. Neff, P. von Neumann-Cosel, and A. Richter, Phys. Rev. Lett. **98**, 032501 (2007).

[13] M. Seya, M. Kohno, and S. Nagata, Prog. Theor. Phys. **65**, 204 (1981).
[14] W. von Oertzen, Z. Phys. A **354**, 37 (1996); **357**, 355 (1997).
[15] N. Itagaki and S. Okabe, Phys. Rev. C **61**, 044306 (2000).
[16] Y. Kanada-En'yo, H. Horiuchi, and A. Doté, Phys. Rev. C **60**, 064304 (1999).
[17] Y. Kanada-En'yo, M. Kimura, and H. Horiuchi, C. R. Phys. **4**, 497 (2003).
[18] Y. Kanada-En'yo, M. Kimura, and A. Ono, Prog. Theor. Exp. Phys. **2012**, 01A202 (2012).
[19] N. Itagaki, S. Okabe, K. Ikeda, and I. Tanihata, Phys. Rev. C **64**, 014301 (2001).
[20] B. J. Greenhalgh *et al.*, Phys. Rev. C **66**, 027302 (2002).
[21] H. G. Bohlen *et al.*, Phys. Rev. C **68**, 054606 (2003).
[22] W. von Oertzen *et al.*, Eur. Phys. J. A **21**, 193 (2004).
[23] N. I. Ashwood *et al.*, Phys. Rev. C **70**, 064607 (2004).
[24] N. Itagaki, W. von Oertzen, and S. Okabe, Phys. Rev. C **74**, 067304 (2006).
[25] D. L. Price *et al.*, Phys. Rev. C **75**, 014305 (2007).
[26] T. Suhara and Y. Kanada-En'yo, Phys. Rev. C **82**, 044301 (2010).
[27] N. Furutachi and M. Kimura, Phys. Rev. C **83**, 021303 (2011).
[28] W. von Oertzen and H. G. Bohlen, C. R. Phys. **4**, 465 (2003).
[29] N. Itagaki, T. Otsuka, K. Ikeda, and S. Okabe, Phys. Rev. Lett. **92**, 142501 (2004).
[30] N. Furutachi, M. Kimura, A. Doté, Y. Kanada-En'yo, and S. Oryu, Prog. Theor. Phys. **119**, 403 (2008).
[31] M. Kimura, Phys. Rev. C **75**, 034312 (2007).
[32] M. Kimura and N. Furutachi, Phys. Rev. C **83**, 044304 (2011).
[33] J. F. Berger, M. Girod, and D. Gogny, Comput. Phys. Commun. **63**, 365 (1991).
[34] M. Kimura, Phys. Rev. C **69**, 044319 (2004).
[35] D. L. Hill and J. A. Wheeler, Phys. Rev. **89**, 1102 (1953).
[36] Y. Kanada-En'yo, Phys. Rev. C **71**, 014310 (2005).
[37] H. Sagawa, X. R. Zhou, X. Z. Zhang, and T. Suzuki, Phys. Rev. C **70**, 054316 (2004).
[38] J. M. Yao, J. Meng, P. Ring, Z. X. Li, Z. P. Li, and K. Hagino, Phys. Rev. C **84**, 024306 (2011).
[39] T. Suhara and Y. Kanada-En'yo, Phys. Rev. C **84**, 024328 (2011).
[40] N. Imai *et al.*, Phys. Rev. Lett. **92**, 062501 (2004).
[41] H. J. Ong *et al.*, Phys. Rev. C **73**, 024610 (2006).
[42] H. J. Ong *et al.*, Phys. Rev. C **78**, 014308 (2008).
[43] M. Wiedeking *et al.*, Phys. Rev. Lett. **100**, 152501 (2008).
[44] M. Petri *et al.*, Phys. Rev. C **86**, 044329 (2012).